Atmospheric Absorption Model for Dry Air and Water Vapor at Microwave Frequencies below 100 GHz Derived from Spaceborne Radiometer Observations

Frank J. Wentz and Thomas Meissner

Remote Sensing Systems, 444 Tenth Street, Suite 200, Santa Rosa, CA 95401, USA

RSS Technical Report: 103015
Document submitted to Radio Science, Nov 13, 2015

Key Points:

- Water vapor absorption model
- Oxygen absorption model
- Radiative transfer modeling

Abstract

The Liebe and Rosenkranz atmospheric absorption models for dry air and water vapor below 100 GHz are refined based on an analysis of antenna temperature (T_A) measurements taken by the Global Precipitation Measurement Microwave Imager (GMI) in the frequency range 10.7 to 89.0 GHz. The GMI T_A measurements are compared to the T_A predicted by a radiative transfer model (RTM), which incorporates both the atmospheric absorption model and a model for the emission and reflection from a rough-ocean surface. The inputs for the RTM are the geophysical retrievals of wind speed, columnar water vapor and columnar cloud liquid water obtained from the satellite radiometer WindSat. Only modest adjustments to the Liebe and Rosenkranz absorption models are required to achieve consistency with the RTM. The largest adjustments are a decrease in the vapor continuum of 3% to 10%, depending on vapor, and an increase in the dry air absorption being a maximum of 20% at the 89 GHz, the highest frequency considered here. In addition, minor adjustments are made to the strength and shape of the 22.235 GHz vapor line and to the non-resonant oxygen absorption. In addition to the RTM comparisons, our results are supported by a comparison between columnar water vapor retrievals from 12 satellite microwave radiometers and GPS retrieved water vapor values. This study does not considering the 50-70 GHz band of densely spaced oxygen lines, and no modifications are made to these line parameters.

Index Terms:

6969 Remote sensing; 0360 Radiation: transmission and scattering; 6964 Radio wave propagation.

1. Introduction

In the absence of clouds and rain, the absorption and re-emission of microwave radiation propagating through the Earth's atmosphere is governed by the absorption coefficients for dry air, including molecular oxygen and nitrogen, and for water vapor: α_D and α_V. The specification of these two coefficients as functions of radiation frequency f (GHz), air temperature T_a (K), dry air pressure p (kPa), and water vapor pressure e (kPa) has been the subject of investigation since *Becker and Autler* [1946], *Van Vleck* [1947], and *Birnbaum* [1953].

Here we investigate these α_D and α_V functionalities using satellite measurement of the microwave radiation upwelling from the Earth. The most accurate radiative transfer model (RTM) for this Earth radiation is for rain-free observations over the oceans. Furthermore, the ocean surface is radiometrically cold (≈90 K for horizontal polarization at the lower microwave frequencies), and this cold surface provides a high contrast for observing variations in α_D and α_V. For example, a change in α_D or α_V of 0.00005 km^{-1} (0.0002 dB/km) produces a change of about 0.1 K in the ocean brightness temperature (T_B) seen by a microwave radiometer onboard a satellite. The 0.1 K precision is typical of todays' advanced satellite microwave radiometers particularly after averaging over millions of space-based observations [*Wentz and Draper*, 2015]. The sensitivity of 0.00005 km^{-1} is much higher than is generally reported in the extensive literature on α_D and α_V [*Liebe*, 1981; 1985; 1989; *Clough et al*., 1989; *Liebe et al*., 1992; *Rosenkranz*, 1998; *Tretyakov et al*., 2005; *Payne et al*., 2008; 2011].

Taking advantage of this high sensitivity, we have derived new expressions for α_D and α_V. This derivation is based on satellite T_B observations in the 11 to 89 GHz range. Our primary goal

is to improve the atmospheric absorption model so it can be used together with our surface emission model [*Meissner and Wentz*, 2004; 2012] to form a complete and accurate RTM for the ocean surface and intervening atmosphere. This RTM can then be used for analysis and calibration of past, present, and future spaceborne MW sensors. We are not considering sounding channels that operate within the 50-70 GHz band of densely spaced oxygen lines. These oxygen lines are excluded from our analysis, and we only study the continuum parts of α_D. The coefficients α_D and α_V are derived such that the ocean RTM T_B equals satellite measurements of T_B over the full range of water vapor values (i.e., from the tropics to the cold, dry polar regions). We find that only modest adjustments to the α_D and α_V expressions reported by *Liebe* [1989], *Liebe et al*. [1992], and *Rosenkranz* [1998] are required to achieve a precise match between model and measurements.

2. Formulation

In the absence of rain, the ocean brightness temperature T_B as seen by an orbiting satellite instrument is given by:

$$\begin{aligned} T_B &= T_{BU} + \tau(0,H)\left[ET_s + (1-E)\left(T_{BD} + \tau(0,H)T_{B,space}\right)\right] + \tau(0,H)T_{B,scat} \\ T_{B,scat} &= \Omega(1-E)\left[T_{BD} + \tau(0,H)T_{B,space} - T_{B,space}\right] \end{aligned} \quad (1)$$

Here T_{BU} and T_{BD} are the upwelling and downwelling atmospheric brightness temperatures, $T_{B,space}$ is the temperature of the cosmic microwave background radiation (cold space), $\tau(0,H)$ is the total transmittance through the atmosphere, E and T_s are the emissivity and temperature of the ocean surface, and H is the height at which the atmospheric absorption is effectively zero. For the microwave frequencies considered here, H = 12 km. The sea-surface emissivity E is a function of wind speed W and wind direction φ_w. The term $T_{B.scat}$ which is proportional to the

empirical factor Ω term is a small adjustment that accounts for scattering as opposed to reflections from the sea surface, as discussed by *Wentz and Meissner* [2000] and *Meissner and Wentz* [2012]. The upwelling and downwelling T_B are found by integration through the atmosphere

$$T_{BU} = \sec\theta_i \int_0^H dh\alpha(h) T_a(h) \tau(h,H) \tag{2}$$

$$T_{BD} = \sec\theta_i \int_0^H dh\alpha(h) T_a(h) \tau(0,h) \tag{3}$$

where θ_i is the angle between the satellite viewing direction and the Earth's geoid and is called the Earth incidence angle, h is the height (km) above the Earth's surface, $\alpha(h)$ is the atmospheric absorption coefficient, $T_a(h)$ is the air temperature, and $\tau(h_1,h_2)$ is the atmospheric transmission function given by

$$\tau(h_1,h_2) = \exp\left(-\sec\theta_i \int_{h_1}^{h_2} dh\alpha(h)\right) \tag{4}$$

The atmospheric absorption coefficient (km^{-1}) consists of three components: dry air, water vapor, and cloud water.

$$\alpha(h) = \alpha_D(h) + \alpha_V(h) + \alpha_C(h) \tag{5}$$

Wentz [1983, 1997] shows that the integrals in (2), (3), and (4) can be well approximated by analytical expressions that are functions of sea-surface temperature T_S, columnar water vapor V, and columnar cloud liquid water C.

$$V = \int_0^H dh\rho_V \tag{6}$$

where ρ_V is water vapor density. A similar expression holds for C.

3. Inputs to RTM

The calculation of T_B requires the following model inputs: T_s, φ_w, W, V and C. T_s comes from the NOAA SST operational product [Reynolds et al., 2002], and φ_w comes the NCEP 6-hour wind fields. The sensitivity of T_B to φ_w is small, and when the data are averaged, any errors in φ_w become negligible for the type of analysis we are presenting here. The remaining environmental parameters (W, V, and C) come from the satellite observations via a geophysical retrieval algorithm. For our analysis, the most important of these parameters is V.

We compute the ocean surface emissivity E component of the RTM from T_s, W and φ_w using the dielectric model of *Meissner and Wentz* [2004] and our rough surface emission model [*Meissner and Wentz*, 2004; 2012].

The vapor retrieval algorithm was initially developed using radiosonde observations as the absolute calibration reference [*Wentz*, 1997]. The retrieval algorithm evolved over time, and a recent study by *Mears et al.* [2015] reported on an extensive comparison of the satellite-derived V with that derived from the vapor-dependent delay of GPS satellite radio signals. Vapor data from nine satellite microwave radiometers spanning 25 years were used in the comparisons. The standard deviations for individual GPS matchups were found to be 2 mm or less. When averaged over many matchups, the systematic error, excluding overall bias, was about 0.5 mm from 0 to 60 mm of vapor. Based on this GPS analysis, we expect the accuracy of the columnar vapor for our analysis to be of a similar accuracy when sufficiently averaged.

The wind algorithm was likewise developed and also has been thoroughly evaluated [*Wentz* 1997; *Mears et al*., 2001; *Wentz,* 2015]. In this case, it was ocean buoy wind speeds that are the absolute calibration reference. Comparisons of radiometer wind speeds with moored buoy observations typically show standard deviations near 1 m/s for individual matchups. However, some of this error is due to the spatial/temporal mismatch between the buoy point observation and the much larger field of view of the satellite (20-50 km). Also, the satellite 'wind' retrieval is more of a measure of surface roughness than the actual wind speed at 5 to 10 m above the surface. For this analysis, W is only used to find the sea surface emissivity E, and hence it is to our advantage that W is more of a roughness indicator than a wind speed indicator. Collocation of W from pairs of satellite radiometers typically show a standard deviation of 0.7 to 0.8 m/s. This suggests that the accuracy of W when interpreted as an indicator of roughness is $0.75/\sqrt{2} = 0.5$ m/s. When averaged over millions of observations, the error related to W is very small.

For the cloud algorithm, we do not have a good absolute calibration reference other than clear skies, for which C=0. The fact that a high percentage of observations are clear skies allows us to use a histogram technique to evaluate the cloud retrieval. An ensemble of cloud histograms are generated for various stratifications of T_s, V, and W. These cloud histograms are all required to have the same alignment for C=0. *Wentz* [1997] used this technique to demonstrate that the self-broadening water vapor continuum absorption α_V of *Liebe* [1985] at 37 GHz was about 20% too high, a problem also detected later by *Payne et al*. [2011]. The evidence for this was that the cloud retrievals from the Special Sensor Microwave Imagers (SSM/I) showed an obvious error that was directly related to V. At high water vapor, the cloud retrievals were negative. This was due to the vapor continuum being too large and in turn the vapor correction to the cloud retrieval

was too large, resulting in an overcorrection that biased the cloud values low. In addition to the C=0 alignment requirement, the cloud algorithm relies on the Rayleigh scattering approximation to specify α_C and the permittivity of liquid cloud water [*Meissner and Wentz*, 2004].

4. Satellite versus Model Comparisons

To compare the model brightness temperature (1) to satellite observations, the antenna characteristics of the satellite microwave radiometer must be considered. The antenna temperature T_A measured by the radiometer is given by

$$T_{Av,rtm} = (1-\eta)\frac{T_{Bv} + \chi T_{Bh}}{1+\chi} + \eta T_{B,space} \tag{7}$$

where we have now introduced polarization notation, with subscripts *v* and *h* denoting vertical and horizontal polarization, respectively. Polarization comes into (1) due to the surface emissivity E being polarized. The subscript *rtm* denotes this T_A is computed from the radiative transfer model described above. The term η is the antenna spillover, which is the fraction of received power coming from cold space as opposed to coming from Earth. The term χ is the fraction of orthogonally polarized power that is received. $T_{B,space}$ is near 2.73 K. Its effective value that is used in the computation accounts for the deviation of the Rayleigh-Jeans approximation from the Planck law and depends on frequency [*Meissner et al.*, 2012]. The h-pol T_A is also given by (7), but with the *v* and *h* subscripts reversed.

For the satellite T_A measurements, we use those obtained from the microwave radiometer that flies on NASA's Global Precipitation Mission (GPM) Core Observatory. The sensor, called GMI for GPM Microwave Imager, is the first satellite microwave imager to employ a dual on-board calibration system. In addition to a mirror viewing cold space and a black-body hot load,

GMI also has noise diodes to provide redundant calibration and a direct measurement of the sensor's non-linearity. Several orbital maneuvers were performed to establish an absolute calibration of T_A near 0.2 K [*Wentz and Draper*, 2015]. GMI has 14 channels ranging from 11 GHz to 183 GHz. Here, we only consider the 9 lower channels that go up to 89 GHz. The atmospheric absorption for the higher frequencies of 166 GHz and 183 GHz is very large, and the RTM computation is very sensitive to the details of vapor and temperature profiles. The GMI T_A measurements are denoted by $T_{A,gmi}$. The values for GMI η and χ are given by *Wentz and Draper* [2015].

For this analysis, the first 13 months of GMI observations (March 2014 through March 2015) are used. Since the analysis requires *W*, *V*, and *C* retrievals, we need geophysical retrievals from a second satellite instrument at nearly the same time and location as the GMI T_A observations. For this, we use the geophysical retrievals from the microwave imager WindSat that flies on the Navy's Coriolis satellite. The collocation criterion is that WindSat ocean retrievals are rain free, are within ± one hour of the GMI T_A observation, and are within a spatial collocation window of 25 km.

We consider WindSat to be the best calibrated sensor that is collocated with GMI. The WindSat ocean retrievals have been thoroughly validated by *Wentz* [2015] and many others [*Meissner et al*., 2011; *Mears et al.*, 2015; *De Biasio and Zecchetto*, 2013; *Huang et al*., 2014] against buoy measurements, GPS vapor measurements, and geophysical retrievals for other satellites. WindSat has proven to be a very stable sensor. Comparisons of WindSat SST and winds

with ocean buoys and WindSat vapor with GPS-derived vapor show no obvious evidence of drift. Comparisons with TMI also verify the stability of WindSat [*Wentz*, 2015].

5. Adjustments to the Dry Air and Vapor Absorption Coefficients

Our derivation of α_D and α_V is based on an analysis of the measured-minus-modeled T_A differences.

$$\Delta T_A = T_{A,gmi} - T_{A,rtm} \tag{8}$$

Figure 1 shows ΔT_A plotted versus columnar water vapor V. Each frame corresponds to one of the 9 lower frequency GMI channels. The red curves are the results obtained when using the dry air coefficient given by *Liebe* [1989] and *Liebe et al*. [1992] and the vapor coefficient given by *Rosenkranz* [1998]. For the dry air coefficient, the formulation is from *Liebe* [1989] but the numerical values of the parameters in the formulation are taken from *Liebe et al*. [1992]. The most obvious feature in the plot is the strong negative slope of ΔT_A at the higher frequencies. This is due to the same problem mentioned above: the water vapor continuum is too strong at higher frequencies. The unmodified *Rosenkranz* [1998] vapor continuum in terms of km^{-1} is

$$\alpha_{Vc} = 0.41907 \times 10^{-1} f^2 \theta^3 \left(a_1 pe + a_2 \theta^{4.5} e^2 \right) \tag{9}$$

where the dimensionless term θ is 300/T_a. The coefficients a_1 (foreign-broadening part) and a_2 (self-broadening part) were derived from best fits to laboratory measurements. The values are 1.296E-6 and 4.295E-5, respectively. We found the following modification to the a_1 and a_2 coefficients removed the correlation of ΔT_A with V over the frequency range from 19 to 89 GHz

$$\alpha'_{Vc} = 0.41907 \times 10^{-1} f^2 \theta^3 \left(1.1 a_1 pe + 0.425 f^{0.1} a_2 \theta^{4.5} e^2 \right) \tag{10}$$

where we use the prime sign to indicate the modified coefficient. For typical water vapor values near 25 mm, the modification is about a 3% reduction. At high values near V = 50 mm, the reduction is about 10%. This reduction is considerably less than the 20% reduction that was required for the *Liebe* [1985] model in *Wentz* [1997]. Our adjusted water vapor continuum absorption model (10) is in very good agreement with the results of *Payne et al*. [2011].

A much smaller adjustment is made to the 22 GHz vapor line shape. Looking at comparisons of satellite water vapor retrievals with radiosondes and vapor values derived from GPS satellites, we conclude that a 1% increase in the strength of the 22 GHz line gives slightly better agreement over the full range of V from 5 to 65 mm.

$$S'_{22.235} = 1.01 S_{22.235} \tag{11}$$

We also find that after applying the adjustments to the dry air absorption, to be discussed below, there was a small residual correlation of ΔT_A with V at 11 GHz. This is corrected by slightly increasing the low-frequency wing of the line. Noting that the Gross line shape [*Gross*, 1955] has more absorption in the low-frequency wing than does the Van Vleck-Weisskopf shape [*Van Vleck and Weisskopf*, 1945], we transform the Van Vleck-Weisskopf shape to the Gross shape at the lower frequencies using the following generalized line shape [*Ben-Reuven*, 1965; 1966]:

$$\phi(f) = \frac{2}{\pi}\frac{f}{f_o}\frac{(\gamma-\chi)f^2 + (\gamma+\chi)\left(f_o^2+\gamma^2-\chi^2\right)}{\left(f^2 - f_o^2 - \gamma^2 + \chi^2\right)^2 + 4f^2\gamma^2} \tag{12}$$

where γ is the line half width, f_o is the center frequency (22.2351 GHz), and χ is an adjustable parameter. For χ = 0, $\phi(f)$ is the Van Vleck-Weisskopf shape, and for $\chi = \gamma$, $\phi(f)$ is the Gross shape. The following expression, which is applied for 2.5 GHz < f < 19 GHz, smoothly transforms the Van Vleck-Weisskopf shape to the Gross shape as f goes from 19 to 2.5 GHz.

$$\chi = \gamma x^2 (3 - 2x) \tag{13}$$

$$x = \frac{19 - f}{16.5} \tag{14}$$

The green line in Figure 1 shows ΔT_A after applying the above corrections to the water vapor continuum and 22 GHz line shape. Changing the water vapor absorption has little or no effect for low vapor values. To remove the ΔT_A bias for the low vapor values, we adjust the dry air absorption. Two changes are made to the *Liebe* [1989] formulation. The first is to the width parameter $\gamma_{O,nr}$ for the nonresonant oxygen absorption, which becomes dominant at very low frequencies. The *Liebe* [1989] value is

$$\gamma_{O,nr} = 0.0056(p + 1.1e)\theta \tag{15}$$

We modified this expression by increasing the θ exponent to 1.5.

$$\gamma'_{O,nr} = 0.0056(p + 1.1e)\theta^{1.5} \tag{16}$$

This slightly increases the dry air absorption, with the increase being essentially independent of frequency for $f > 2$ GHz. The second change is to the pressure-induced nitrogen absorption continuum. It is part of the dry air absorption and becomes noticeable for the higher frequencies. Therefore it needs to be added to the oxygen line absorption and the non-resonant oxygen continuum absorption. The *Liebe* [1989] expression in terms of km^{-1} is

$$\alpha_{Dc} = 0.58670 \times 10^{-11} f^2 p^2 \theta^{3.5} (1 - 1.2 \times 10^{-5} f^{1.5}) \tag{17}$$

To this we add an additional dry air absorption for frequencies above 37 GHz

$$\alpha'_{Dc} = \alpha_{Dc} + 0.10896 \times 10^{-9} p^2 \theta^3 (f - 37)^{1.8} \, u(f - 37) \tag{18}$$

where $u(x)$ is the unit step function. We use a temperature exponent of 3, which is the same as what *Liebe* [1989] used for the strength of the oxygen lines.

The black lines in Figure 1 show ΔT_A after we apply both the water vapor and the dry air adjustments. Comparing the green and black curves shows that modifying $\gamma_{O,nr}$ removes nearly all of the remaining ΔT_A biases for frequencies up to 37 GHz. Above 37 GHz, modification (18) is required to remove ΔT_A biases at low water vapors. With all adjustments applied, ΔT_A is generally within a ±0.2 K envelope, except for some channels at very low and high vapor values. The 11V and 19V ΔT_A both show an upturn for V = 5 mm. These channels are sensitive to T_S and the upturn may be due to an error in the Reynolds T_s in cold water.

We also want to note that the bias that is observed in ΔT_A without the adjustments (red curve in Figure 1) is roughly twice as large for horizontal polarization as for vertical polarization. This relationship suggests that we are dealing with an uncertainty in the atmospheric model rather than an uncertainty in the seawater permittivity model that is used in computing the surface emissivity. For the GMI frequencies and Earth incidence angles, the h-pol reflectivity is about twice as large as the v-pol reflectivity and therefore, according to the RTM equation (1), an error in the atmospheric absorption impacts the h-pol T_B twice as much as the v-pol T_B [*Meissner and Wentz,* 2002; 2012]. If the error was in the water permittivity model it would impact the v-pol more than the h-pol [*Meissner and Wentz,* 2004].

Figure 2 shows α_V and α'_V for typical mid-latitude values of T_a = 275 K, p = 100 kPa, and e = 8 kPa. The figure shows the change to the shape of the Van Vleck-Weisskopf vapor line is very small, and we hesitate to conclude too much. Possibly our results are closer to the true line shape, or possibly our modifications are compensating for other effects not fully understood.

Figure 3 shows α_D and α'_D, again for typical mid-latitude values of T_a, p, and e. Below 37 GHz the small increase in α'_D is due to modifying $\gamma_{O,nr}$, and this change is nearly independent of frequency. Above 37 GHz, modification (18) takes effect and one sees a significant increase in α'_D relative to α_D.

All 5 modifications (Equations 10, 11, 13, 16, 18) had been derived from earlier analyses of the SSM/I, AMSR, and WindSat satellite sensors. GMI, with its advanced calibration system, allows us to verify these prior modifications. The GMI observations support modifications (11), (13), and (16), and there was no need to make any changes to the previously derived values. For modifications (10) and (18), which relate to the vapor and pressure induced nitrogen continuum, the GMI results indicate the prior adjustments were a bit too much. For the vapor continuum adjustment, we had previously used $0.375\, f^{\,0.15}$ rather than $0.425\, f^{\,0.1}$ for modification to the self-broadening a_2 term. Changing the exponent to 0.1 reduces the size of the adjustment (except for at frequencies below 12 GHz for which the adjustment is negligibly small). The prior adjustment term that was added to the pressure induced nitrogen absorption was

$$\alpha''_{Dc} = \alpha_{Dc} + 0.125721\times 10^{-10} f^2 p^2 \theta^3 \qquad (19)$$

where the double prime indicates prior adjustment. The GMI results indicate that no adjustment is needed to the pressure induced nitrogen absorption for frequencies of 37 GHz and below. At 89 GHz, GMI indicates that α_{Dc} needs to be increased by about 17%. So (19) was replaced by (18).

6. Comparison of Satellite Vapor Retrievals with GPS vapors

In addition to requiring ΔT_A be near zero over the full range of V, as is shown in Figure 1, the other requirement is that the satellite vapor retrievals be consistent with the GPS vapors.

Mears et al. [2015] show that this is the case, and Table 1 summarizes the *Mears et al.* [2015] results in term of the slope

$$S_{vap} = \frac{V_{sat} - V_{gps}}{\frac{1}{2}\left(V_{sat} + V_{gps}\right)} \tag{20}$$

where V_{sat} and V_{gps} are the satellite vapor retrieval and the GPS vapor retrieval. Results are shown for 12 satellite sensors. The slope S_{vap} is found by finding collocated pairs of V_{sat} and V_{gps}, and binning the difference according to the average. A least-squares slope S_{vap} is then found for all bins from 0 to 60 mm. S_{vap} does not exceed 1%. Above 60 mm, all sensors, except AMSR-E, show V_{sat} biased low relative to V_{gps} by about 0.5 mm. There is little data above 60 mm, and we are not sure what this bias may be due to.

Liljegren et al. [2005] reported that a decrease of 5% in the *Rosenkranz* [1998] air-broadened half-width γ_{dry} for the 22 GHz vapor line greatly improved the agreement between the Rosenkranz model and brightness temperatures obtained from upward looking radiometers during the February 2000 Atmospheric Radiation Measurement (ARM) experiment at its Southern Great Plains site. This is a much larger modification than reported here. Figure 4 shows the GMI ΔT_A comparisons when γ_{dry} is decreased by 5%. Significant correlations between ΔT_A versus V occur. At 37 GHz, the ΔT_A versus V correlation could be removed by using a slightly different vapor continuum. However, the real problem is at 19 and 24 GHz, for which the correlations have different signs.

The 5% decrease in γ_{dry} would have its most significant effect on the SSM/I and SSMIS vapor retrievals. These two sensor types operate at a frequency 22.235 GHz, which is at the center of the vapor line. At the center frequency, decreasing the γ_{dry} increases the water vapor absorp-

tion by 4% (not 5% because of the continuum contribution). The larger absorption translates into a 4% reduction in the *V* retrievals. Relative to the *V* retrievals we get with the above model, the reduction is only 3% because our model also increases the 22.235 GHz absorption, but only by 1% rather than 5%. A 3% reduction in *V* retrievals would be inconsistent with the GPS comparisons shown in Table 1.

7. Conclusions

Liebe [1989] and *Liebe et al.* [1992] dry air absorption coefficients and the *Rosenkranz* [1998] vapor absorption coefficients require only a modest adjustment to obtain consistency with satellite observations of the upwelling microwave radiation coming from the Earth's atmosphere overlying the oceans. The largest adjustments are a decrease in the vapor continuum of 3% to 10%, depending on vapor, and an increase in the nitrogen absorption being a maximum of 20% at the 89 GHz, the highest frequency considered here. Minor adjustments are made to the 22.235 GHz line shape and the nonresonant oxygen absorption. With these adjustments, the agreement between the satellite observations and the model are generally at the ±0.2 K level, except for some channels at very low and very high vapor values.

References

Becker, G.E., and S.H. Autler, 1946: Water vapor absorption of electromagnetic radiation in the centimeter wave-length range, Physical Review, 70, 300 – 307.

Ben-Reuven, A, 1965: Transition from resonant to nonresonant line shape in microwave absorption, Physical Review Letters, 14, 349 – 351.

Ben-Reuven, A., 1966: Impact broadening of microwave spectra, Physical Review Letters, 145, 7 – 22.

De Biasio, F., and S. Zecchetto, 2013: Comparison of sea surface winds derived from active and passive microwave instruments on the Mediterranean Sea. Presentation EGU2013-10157 at the EGU General Assembly Conference, European Geosciences Union, Vienna, Austria.

Birnbaum, G., 1953: Millimeter wavelength dispersion of water vapor, Journal of Chemical Physics, 21(1), 57 – 61.

Clough, S A., F.X. Kneizys and R.W. Davies, 1989: Line shape and the water vapor continuum, Atmospheric Research, 23, 229 – 241.

Gross, E.P., 1955: Shape of Collision broadened spectral lines, Physical Review, 97, 395 – 403.

Huang, X., et al., 2014: A preliminary assessment of the sea surface wind speed production of HY-2 scanning microwave radiometer, Acta Oceanologica Sinica, 33, 114 – 119.

Liebe, H., 1981: Modeling attenuation and phase of radio waves in air at frequencies below 1000 GHz, Radio Science, 16(6), 1183 – 1199.

Liebe, H.J., 1985: An updated model for millimeter wave propagation in moist air, Radio Science, 20, 1069 – 1089.

Liebe, H.J., 1989: MPM – An Atmospheric Millimeter-Wave Propagation Model, International Journal of Infrared and Millimeter Waves, 10(6), 631 – 650.

Liebe, H.J., P.W. Rosenkranz, and G.A. Hufford, 1992: Atmospheric 60-GHz oxygen spectrum: New laboratory measurements and line parameters, Journal of Quantitative Spectroscopy & Radiative Transfer, 48, 629 – 643.

Liljegren, J.C., S.A. Boukabara, K. Cady-Pereira and S.A. Clough, 2005: The effect of the half-width of the 22-GHz water vapor line on retrievals of temperature and water vapor profiles with a 12-channel microwave radiometer, IEEE Transactions on Geoscience and Remote Sensing, 43(5), 1102 – 1108.

Mears, C.A., D.K. Smith, and F.J. Wentz, 2001: Comparison of Special Sensor Microwave Imager and buoy-measured wind speeds from 1987 – 1997, Journal of Geophysical Research, 106, 11719 – 11729.

Mears, C.A., J. Wang, D.K. Smith, and F.J. Wentz, 2015: Intercomparison of total precipitable water measurements made by satellite-borne microwave radiometers and ground-based GPS instruments, Journal of Geophysical Research: Atmospheres, 120, 2492 – 2504.

Meissner, T., and F.J. Wentz, 2002: An updated analysis of the ocean surface wind direction signal in passive microwave brightness temperatures, IEEE Transactions on Geoscience and Remote Sensing, 40(6), 1230 – 1240.

Meissner, T., and F.J. Wentz, 2004: The complex dielectric constant of pure and sea water from microwave satellite observations, IEEE Transactions on Geoscience and Remote Sensing, 42(9), 1836.

Meissner, T., L. Ricciardulli, and F.J. Wentz, 2011: All-weather wind vector measurements from intercalibrated active and passive microwave satellite sensors. 2011 IEEE International Geoscience and Remote Sensing Symposium (IGARSS), Vancouver, BC, Canada, IEEE, DOI 10.1109/IGARSS.2011.6049354.

Meissner, T., and F.J. Wentz, 2012: The emissivity of the ocean surface between 6 - 90 GHz over a large range of wind speeds and Earth incidence angles, IEEE Transactions on Geoscience and Remote Sensing, 50(8), 3004 – 3026.

Meissner, T., F.J. Wentz and D. Draper, 2012: GMI Calibration Algorithm and Analysis Theoretical Basis Document (ATBD) Version G, report number 041912, Remote Sensing Systems, Santa Rosa, CA, 2012, available at http://www.remss.com/support/publications.

Payne, V.H., J.S. Delamere, K.E. Cady-Pereira, R.R. Gamache, J. Moncet, E.J. Mlawer and S.A. Clough, 2008: Air-broadened half-widths of the 22- and 183-GHz water-vapor lines, IEEE Transactions on Geoscience and Remote Sensing, 46(11), 3601 – 3617.

Payne, V.H., E.J. Mlawer, K.E. Cady-Pereira and J. Moncet, 2011: Water vapor continuum absorption in the microwave, IEEE Transactions on Geoscience and Remote Sensing, 49(6), 2194 – 2208.

Reynolds, R.W., N.A. Rayner, T.M. Smith, D.C. Stokes, and W. Wang, 2002: An improved in situ and satellite SST analysis for climate, Journal of Climate, 15, 1609 – 1625.

Rosenkranz, P., 1998: Water vapor microwave continuum absorption: A comparison of measurements and models, Radio Science, 33, 919 – 928.

Tretyakov, M.Y., M.A. Koshelev, V.V. Dorovskikh, D.S. Makarov and P.W. Rosenkranz, 2005: 60-GHz oxygen band: Precise broadening and central frequencies of fine-structure lines, absolute absorption profile at atmospheric pressure, and revision of mixing-coefficients, Journal of Molecular Spectroscopy, 231(1), 1 – 14.

Van Vleck, J.H. and V.F. Weisskopf, 1945: On the shape of collision-broadened lines, Reviews of Modern Physics, 17, 227 – 236.

Van Vleck, J.H., 1947: The absorption of microwaves by oxygen and uncondensed water vapor, Physical Review, 71(7), 413 – 433.

Wentz, F. J., 1983: A Model Function for Ocean Microwave Brightness Temperatures, Journal of Geophysical Research, 88(C3), 1892 – 1908.

Wentz, F.J., 1997: A well calibrated ocean algorithm for special sensor microwave / imager, Journal of Geophysical Research, 102, 8703 – 8718.

Wentz, F.J., L. Ricciardulli, C. Gentemann, T. Meissner, K. A. Hilburn, and J. Scott, 2013: Remote Sensing Systems Coriolis WindSat Environmental Suite. Daily on 0.25 deg grid, Version 7.0.1, Remote Sensing Systems, Santa Rosa, CA. Accessed 2014 – present. Available online at www.remss.com/missions/windsat.

Wentz, F.J., 2015: A 17-Year Climate Record of Environmental Parameters Derived from the Tropical Rainfall Measuring Mission (TRMM) Microwave Imager, Journal of Climate, 28, 6882 – 6902.

Wentz, F.J. and D. Draper, 2015: On-Orbit Absolute Calibration of the Global Precipitation Mission Microwave Imager. Submitted to Journal of Atmospheric and Oceanic Technology.

Wentz, F.J. and T. Meissner, 2000: AMSR Ocean Algorithm Theoretical Basis Document (Version 2), RSS Tech. Proposal 121599A-1, Remote Sensing Systems, Santa Rosa, CA, December 1999, revised 2000, 66pp, available at http://www.remss.com/support/publications.

Acknowledgements

This work has been supported by NASA's Earth Science Division. We are grateful to Carl Mears, Remote Sensing Systems, for providing the analysis comparing the satellite vapor retrievals with the GPS vapor.

The L1A GMI antenna temperatures are available from NASA's Precipitation Processing System PPS http://pps.gsfc.nasa.gov/. The values for the WindSat wind speed, columnar water vapor and columnar cloud liquid water are from Remote Sensing Systems [*Wentz et al.*, 2013]. The NOAA SST operational product is available from ftp://eclipse.ncdc.noaa.gov/pub/OI-daily-v2/IEEE/YYYY/AVHRR-AMSR, where YYYY is the year 2014 to present.

Table 1. Slope S_{vap} (percentage) for satellite versus GPS vapor comparisons.

F10	F11	F13	F14	F15	F16	F17	AMSR-E	AMSR2	WindSat	TMI	GMI
-0.55	0.03	-0.08	0.23	0.10	-0.14	-0.04	0.91	-0.14	0.16	0.95	-0.30

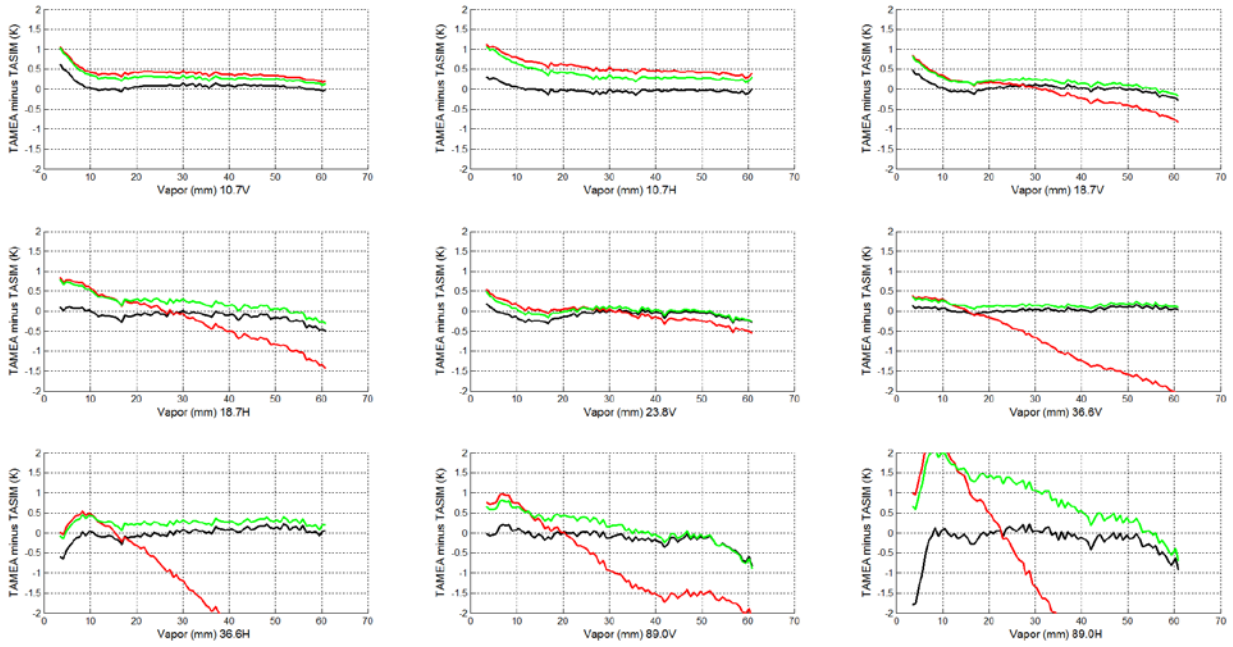

Figure. 1. Measured minus RTM computed antenna temperatures for the 9 lowest GMI channels: Red curves: using the dry air coefficients given by *Liebe* [1989] and *Liebe et al*. [1992] and the vapor coefficients given by *Rosenkranz* [1998]. Green curves: after adjusting the water vapor absorption. Black curves: after adjusting both water vapor and dry air absorption.

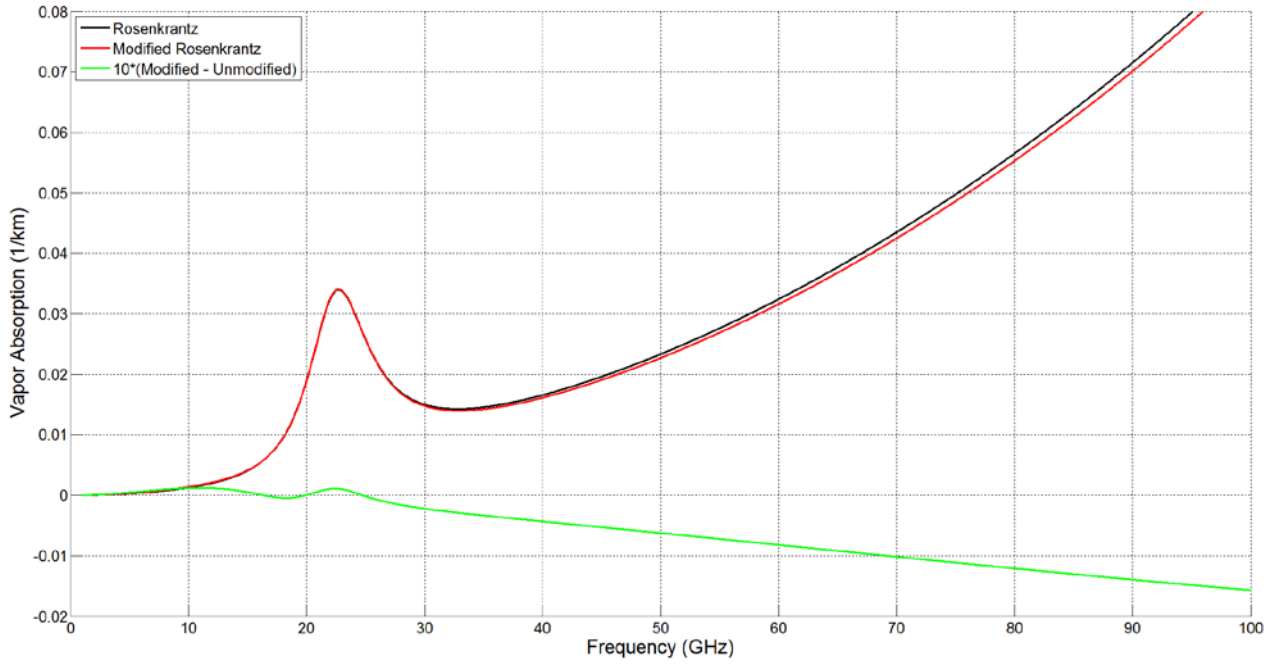

Figure. 2. Total water vapor absorption (km^{-1}) from *Rosenkranz* [1998] (black curve) and after making the adjustments in this paper (red curve). The green curve shows 10-times the difference between the adjusted and unadjusted water vapor absorption model.

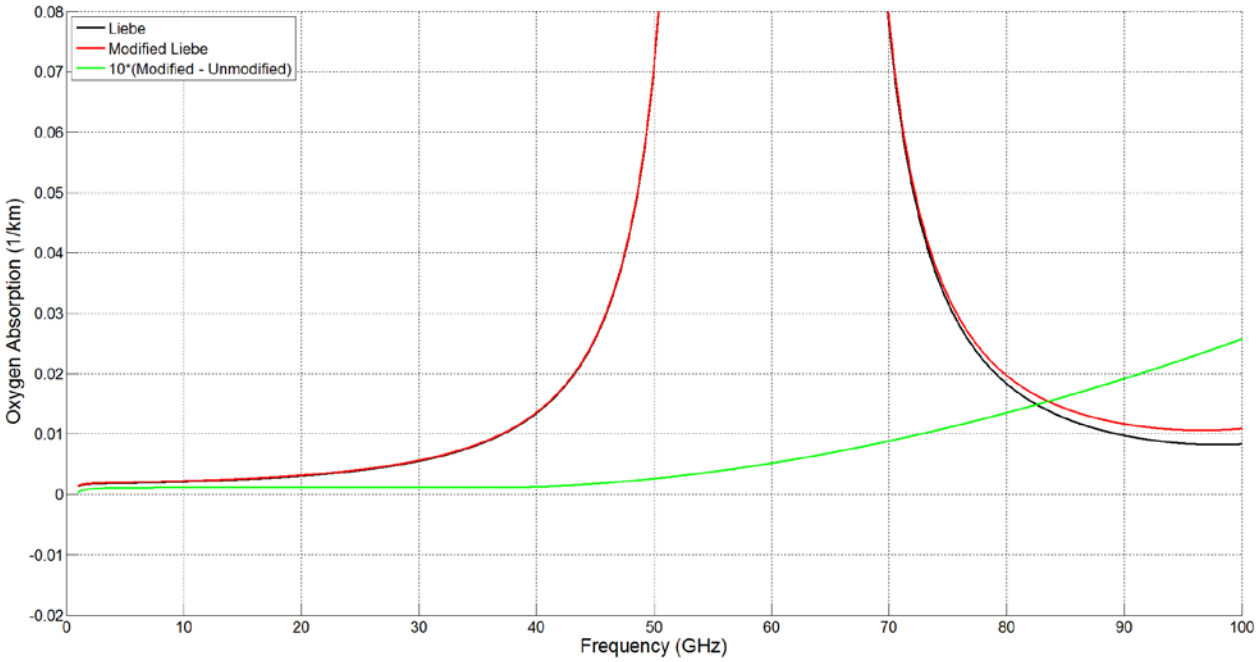

Figure. 3. Total dry air absorption (km^{-1}) from *Liebe et al.* [1992] (black curve) and after making the adjustments in this paper (red curve). The green curve shows 10-times the difference between the adjusted and unadjusted dry air absorption model.

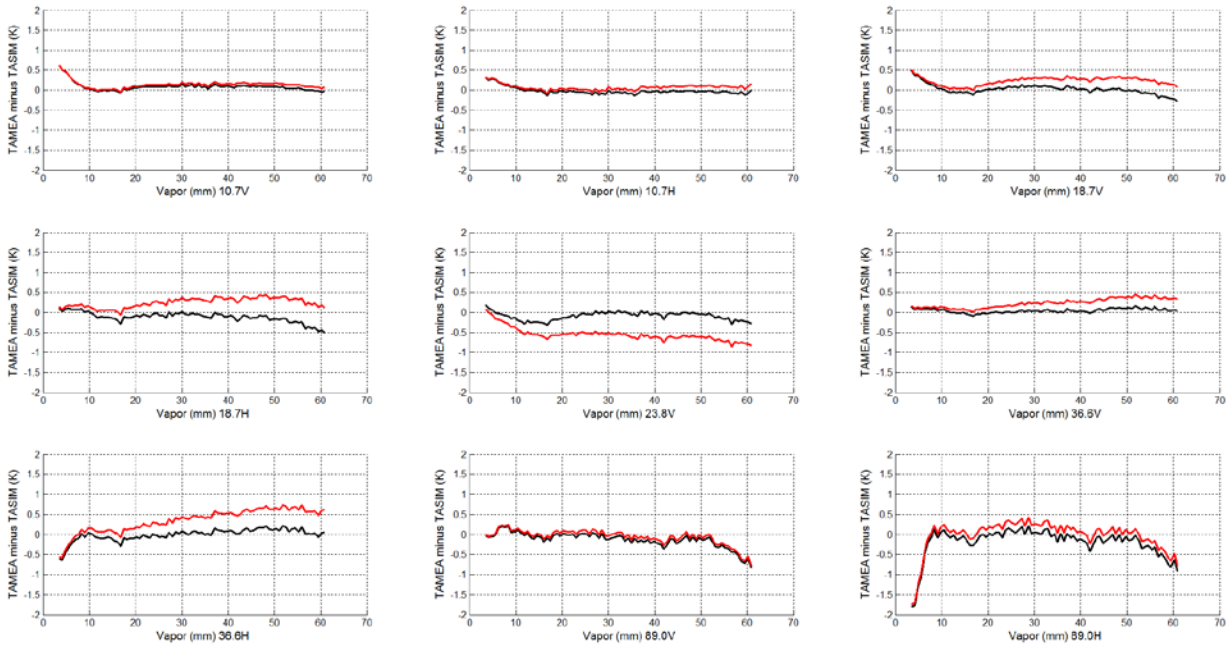

Figure 4. Differences between measured and RTM computed antenna temperatures for the 9 lowest GMI channels. The black curves show the results for the absorption model in this paper (same as in Figure 1). The red curves show the results if the air-broadened half-width for the 22 GHz vapor line is decreased by 5% as suggested in *Liljegren et al*. [2005].